Ab initio calculation of near-edge structures in electron-energy-loss spectra for metal-oxide crystals

S. Köstlmeier and C. Elsässer
Max-Planck-Institut für Metallforschung, Seestraße 92, D-70174 Stuttgart, Germany
(Received 12 August 1998; revised manuscript received 25 May 1999)

The local electronic structure and its relation to the atomic environment of the ions in MgO, $MgAl_2O_4$, and α-Al_2O_3 are analyzed by means of *ab initio* band-structure calculations based on the density-functional theory (DFT). The theoretical results for local densities of states are compared to electron-energy-loss near-edge structures (ELNES) obtained by analytical transmission electron microscopy. For the peak positions of the anionic centers, the validities of the effective one-electron approximation for the crystal potential in the DFT and of the perturbative treatment of single-electron excitations are demonstrated at least semiquantitatively. Limitations in the theoretical treatment for ELNES at the cationic centers are investigated. Improvements are illustrated and discussed in comparison to experimental ELNES data. In particular, this concerns the explicit account for core-hole relaxation effects in the excitation process, and the inclusion of symmetry constraints on the probabilities for the excitations from a core state to conduction-band states. [S0163-1829(99)07543-8]

I. INTRODUCTION

Electron-energy-loss spectroscopy (EELS) has proven to be a valuable method for the investigation of material properties at a microscopic scale (see, e.g., Ref. 1). Especially the energy-loss near-edge structure (ELNES) was found to be sensitive to variations of the chemical environment of a given element. To name a few examples, ELNES data have been successfully employed to study the distribution of dopants,[2] segregation phenomena at grain boundaries,[3] or electron transfer processes at heterophase interfaces[4–6] (for a recent survey see, e.g., Ref. 1, p. 301 ff).

The analysis of experimental ELNES data is usually based on the comparison of the observed spectrum to data from a set of reference materials and yields information only through changes relative to such a standard.[5,7–9] Theoretical investigations of electronic structures, on the other hand, provide a fundamental tool for the interpretation of structural and electronic changes. Therefore, several attempts have been made to link theory and experiment by calculating the ELNES in analogy to x-ray excitation processes[10–16] to employ these results for the analysis of the experimental ELNES.[17–23] For this purpose, the measured energy-loss intensity $I(E)$ can be related to the square of the transition matrix element $|M(E)|^2$ for a single-electron excitation and the density of unoccupied electron states $N_u(E)$ through Fermi's golden rule (see, e.g., Ref. 10).

Both quantities $M(E)$ and $N_u(E)$ are accessible by electronic-structure calculations. A recent overview of the common theoretical approaches is given in the introduction of Ref. 22. Most prominently, they are based on real-space cluster models, like multiple-scattering (MS) or molecular-orbital methods, or on reciprocal-space band-structure (BS) theory for crystals (for reviews see, e.g., Refs. 1, 24, and 25).

In the present study self-consistent density-functional[26,27] BS calculations were performed to determine the density of states (DOS) $N_u(E)$ for a set of metal-oxide crystals by means of a mixed-basis pseudopotential method.[28–31] This method employs norm-conserving ionic pseudopotentials for the representation of the atom cores. An explicit treatment of the inner-shell electrons is not required in the procedure outlined here, because only conduction-band densities of states are used for the analysis of the ELNES. A mixed-basis set of plane waves and local orbitals represents the one-electron wave functions in the self-consistent solution of the Kohn-Sham equations. Site- and angular-momentum-resolved partial DOS (PDOS) are obtained from the total DOS by projection onto atom-centered partial waves with angular dependencies given by spherical harmonics $Y_{lm}(\theta,\phi)$. The method will be described concisely in Sec. II.

A clear correlation of shapes can be observed between the measured ELNES intensity of the O *K* edge in crystalline oxides and the PDOS of the unoccupied single-electron states projected on the O site for an angular momentum of $l=1$, as will be demonstrated in Sec. III. This correlation will be employed to determine and analyze characteristic O *K*-edge fingerprints for the local environment of the strongly scattering anion centers in different crystal structures.

For the calculation of the ELNES at the weakly scattering cation centers of main-group-metal oxides some refinements must be performed in the site and angular-momentum projection of the density of states. These concern both the cation *K* and *L* edges, but stem from different physical origins, namely core-hole relaxations, spin-orbit, and crystal-field splittings, which will be addressed in Sec. IV.

II. COMPUTATIONAL METHOD

A. Pseudopotential band-structure calculation

For the crystals MgO, α-Al_2O_3, and $MgAl_2O_4$ self-consistent density-functional[26,27] calculations were carried out, employing the conceptually simple X_α approximation[32] as well as the more accurate local-density functional of Perdew and Zunger,[33] based on electron-gas data of Ceperley and Alder,[34] and the gradient-corrected functional of Perdew

and Wang[35–37] for exchange-correlation (XC) interactions. The core-valence interactions were accounted for by norm-conserving ionic pseudopotentials generated according to a scheme of Vanderbilt[38] for the following atomic valence reference configurations: O ($s^2p^{3.75}d^{0.25}$); Mg ($s^{1.5}p^{0.25}d^{0.25}$); Al ($s^2p^{0.75}d^{0.25}$). The Kohn-Sham equations were solved for the valence electron Bloch states $\psi_{n\mathbf{k}}(\mathbf{r})$ with eigenvalues $E_{n\mathbf{k}}$ represented in a mixed-basis set of plane waves and additional local orbitals for p states of O (Refs. 28–31) [numbers of valence electrons per atom: $n(\mathrm{O})=6$, $n(\mathrm{Mg})=2$, $n(\mathrm{Al})=3$].

The smallest possible unit cells were used for the calculations, and three-dimensional periodic boundary conditions ensure that the space-group symmetry of the whole crystal is included properly in the calculation. These were face-centered cubic Bravais lattice cells containing two atoms for MgO (rocksalt structure[39]) and 14 atoms for $MgAl_2O_4$ (two formula units, normal spinel structure[40]). α-Al_2O_3 was represented by a rhombohedral unit cell composed of ten atoms with trigonal symmetry (corundum structure[41]). Unless stated otherwise in the text, all theoretical results were obtained for these small unit cells.

All experimental spectra, that are given in the following figures for comparison to our calculated results, were recorded on a dedicated scanning transmission electron microscope installed at the MPI für Metallforschung in Stuttgart: STEM, VG HB501 UX, 100 keV, equipped with a Gatan 666 PEELS. The spectra were recorded with energy dispersions of 0.1 eV/channel for the O K edges, and of 0.3 eV/channel for both cation-K and -$L_{2,3}$ edges, and analytical background functions were subtracted (courtesy of Müllejans and Duscher; for more details on the experimental technique see, e.g., Ref. 42).

B. Approximate calculation of ELNES

In the EELS process a part of the incident electron beam experiences inelastic scattering with the sample, leading to excitations of both core and valence electrons at the scattering center. Using Bethe's theory for inelastic scattering (see, e.g., Ref. 10) the intensity $I(E)$ in the near-edge region can be shown to be proportional to the square of the transition matrix elements $M(E)$ and the density of unoccupied, final states $N_u(E)$ as given by Fermi's golden rule:

$$I(E)\propto N_u(E)|M(E)|^2. \tag{2.1}$$

The following four assumptions are made for the conceptually simplest stage of the present approach to calculate ELNES. (1) The individual electrons occupy and are excited between single-electron states (one-electron approximation). (2) The transitions between the single-electron states are assumed to happen instantaneously, i.e., within an infinitesimally short time interval. (3) The validity of the dipole approximation is assumed for the transitions. (4) The dependence of the transition matrix element on the energy and on the spatial characteristics of initial and final states is neglected.

The single-electron states of approximation (1) are calculated from self-consistent effective ground-state one-electron potentials of the density-functional theory. (Different exchange-correlation approximations have been considered, see Sec. III A.) To go beyond assumption (1) requires the calculation of quasiparticle spectra instead of single-electron spectra. This has become feasible in recent years by means of the GW approach.[43,44] Its application to covalent and ionic bulk materials has been very successful, but for defect structures like surfaces or grain boundaries, the GW approach is still computationally rather costly. However, relative differences between calculated quasiparticle and single-electron energy dispersion curves for conduction-band states are rather delicate (see, e.g., Refs. 45 and 46) and thus not so important for ELNES. Therefore the single-electron approach investigated in the present work, and intended for ELNES studies of defect structures, can be justified at least as a reasonable approximative methodology for ionic metal oxides.[47]

Assumption (2) means that for initial and final states of the excitation, one-electron states from the same (initial) ground-state effective one-electron potential are used. It can be improved by accounting for final-state effects due to core-hole relaxations. This issue will be discussed in Sec. IV. Assumptions (3) and (4) concern the matrix elements $M(E)$ and will be addressed below after considering site- and angular-momentum resolved PDOS. In Fermi's golden rule [Eq. (2.1)] the matrix elements select the appropriate combination of PDOS compatible with the dipole approximation [assumption (3)] and crystal-field symmetry (see Sec. IV B).

All-electron and pseudopotential BS calculations yield the total densities of states [DOS, $N(E)$] in a self-consistent crystal potential:

$$N(E)=\sum_{n,\mathbf{k}}\delta(\varepsilon-\varepsilon_{n,\mathbf{k}})=\sum_{n,\mathbf{k}}|\langle\psi_{n,\mathbf{k}}|\psi_{n,\mathbf{k}}\rangle_\Omega|^2\quad\delta(\varepsilon-\varepsilon_{n,\mathbf{k}}), \tag{2.2}$$

where $\langle|\rangle_\Omega$ denotes the spatial norm integral over the whole unit cell. All states up to the Fermi level are occupied by electrons [$N_o(E)$] and are not directly involved in core loss spectroscopy. The unoccupied part of the DOS [$N_u(E)$] at energies above the Fermi level is the first factor in relation (2.1) For the analysis of bonding interactions it is useful to decompose this DOS into its angular-momentum components by a projection onto partial waves within a sphere S_α around an atomic site α, where:

$$N^\alpha(E)=\sum_{n,\mathbf{k}}|\langle\psi_{n,\mathbf{k}}|\psi_{n,\mathbf{k}}\rangle_{S_\alpha}|^2\delta(\varepsilon-\varepsilon_{n,\mathbf{k}})=\sum_{l,m}N^{\alpha lm}(E) \tag{2.3}$$

with

$$N^{\alpha lm}(E)=\sum_{n,\mathbf{k}}|\langle\chi^{\alpha lm}_{n\mathbf{k}}|\chi^{\alpha lm}_{n\mathbf{k}}\rangle_{S_\alpha}|^2\delta(\varepsilon-\varepsilon_{n\mathbf{k}}), \tag{2.4}$$

where $\langle|\rangle_{S_\alpha}$ denotes a norm integral over a sphere centered at the atomic site α, and $\psi_{n,\mathbf{k}}$, in general, can be expanded in a set of partial waves at site α:

$$\psi_{n,\mathbf{k}}(\mathbf{r})=\sum_{l,m}\chi^{\alpha lm}_{n\mathbf{k}}(\mathbf{r}-\mathbf{R}_\alpha). \tag{2.5}$$

Thus one obtains *s*-, *p*-, and *d*-type PDOS separately at the specific site α, which are used to fulfill selection rules resulting from the dipole approximation and from crystal-field symmetry. The property of norm conservation in pseudopotential theory[25] warrants that projections of the DOS on atom-centered spheres are the same in all-electron and pseudopotential calculations to a high degree of accuracy, as long as the sphere radii S_α are larger than the cutoff radii for the corresponding atomic valence pseudo-wave-functions.

The second factor in relation (2.1), the transition matrix element for a one-electron excitation, is given by

$$M(E)=\int \psi_f^*(\mathbf{r})e^{-i\mathbf{q}\cdot\mathbf{r}}\psi_i(\mathbf{r})d^3r \qquad (2.6)$$

where $\psi_i(\mathbf{r})$ and $\psi_f(\mathbf{r})$ are the initial- and final-state wave functions of the excited electron and $\mathbf{q}=\mathbf{k}_i-\mathbf{k}_f$ is the momentum transferred during the scattering event ($\mathbf{k}_i$ and $\mathbf{k}_f$ are the wave vectors of the scattered electron before and after the EELS process). More accurately, the transition matrix elements $M(E)$ depend on the energy loss and also on the atomic site α and the angular momenta l and m of $\psi_i(\mathbf{r})$ and $\psi_f(\mathbf{r})$.

The calculation of $M(E)$ is straightforward with all-electron BS methods, which provide wave functions for both initial core and final conduction-band states. With pseudopotential BS methods, on the other hand, the core states are not calculated explicitly for crystals, but included implicitly in the ionic pseudopotentials.[25] For the conduction-band as well as valence-band states the pseudo-wave-functions are calculated instead of the all-electron wave functions. By construction of norm-conserving ionic pseudopotentials, both wave functions coincide in the interstitial volume regions of crystals and thus are equally well suited for density-functional total-energy and force calculations of structure and bonding properties. In the volume regions of overlap with the core states, they are different in shape but equal in norm. [Only the latter is needed for the PDOS $N^{\alpha lm}(E)$, cf. Eq. (2.4).] Hence, in order to calculate matrix elements accurately with a pseudopotential method, the all-electron core and conduction-band wave functions need to be reconstructed. This is possible without much more computational effort, compared to the calculation of pseudo-wave-functions, for instance by means of the technique of Ref. 48.

In the present work, the matrix elements were not calculated explicitly, because their main effect on the ELNES can be assessed by symmetry considerations. Compared to the densities of states, the matrix elements are of minor importance for the following reasons: With the dipole approximation (4), $e^{-i\mathbf{q}\cdot\mathbf{r}}\approx 1-i(\mathbf{q}\cdot\mathbf{r})$, which is natural for x-ray absorption near-edge structures and justified for ELNES with near-parallel scattering, all matrix elements vanish except those for transitions fulfilling the dipole selection rule $\Delta l=\pm 1$. Thus the ELNES is composed of only a few PDOS $N^{\alpha lm}(E)$. For instance, for oxygen *K* edges the O *p* PDOS (discussed in Sec. III and displayed in Figs. 1 and 2) are given by $\Sigma_{m=-1}^{1}N_u^{\alpha 1m}(E)$ with α specifying an oxygen site and $l=1$ the projection on p states. Concerning assumption (4), the spatial characteristics of initial and final states are determined by the radial overlap between the core and conduction-band wave functions, and by the local crystal-field symmetry. The former can be mimicked by a choice of the projection-sphere radius S_α similar to the radial extension of the core-state wave function. The latter leads to another selection rule for Δm, which is obtainable without much computation by group-theoretical considerations. The remaining matrix elements are energy dependent, but in earlier ELNES calculations it was found that this dependence is slowly varying and, thus, not significantly changing the spectral shapes of the ELNES.[49]

Accounting for these assumptions, an at least semiquantitative comparison between experimental and calculated EL-

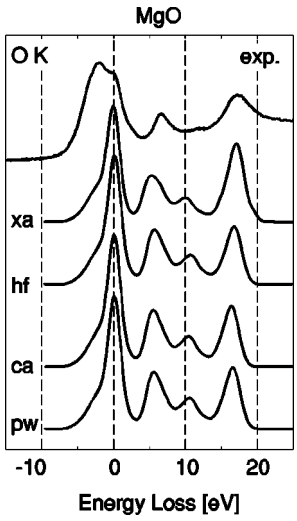

FIG. 1. Oxygen *K* edge in MgO. The experimental spectrum is compared to the unoccupied O *p*-PDOS calculated with the following approximations for the exchange-correlation interaction: Slater's X_α approximation with $\alpha=2/3$ (xa) and $\alpha=1$ (hf), local-density approximation (ca), and generalized gradient approximation (pw). (The ordinate units are arbitrary.)

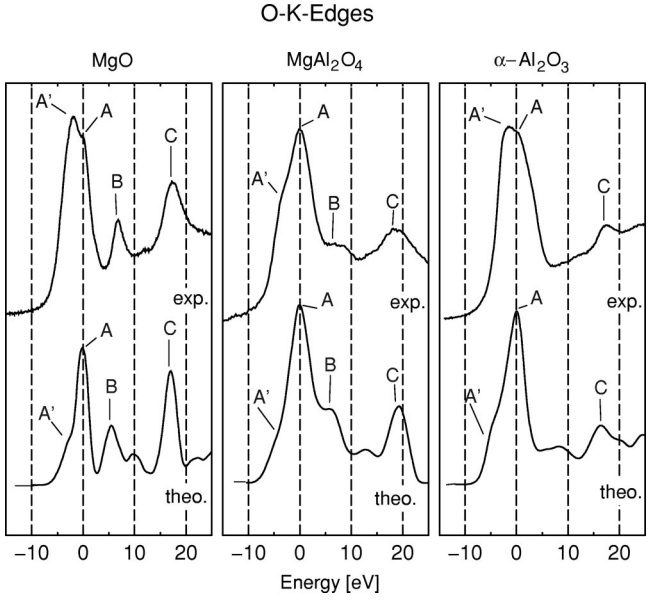

FIG. 2. Comparison of measured O *K* edges (top) of the three oxides MgO (left), $MgAl_2O_4$ (middle), and α-Al_2O_3 (right) and the corresponding calculated unoccupied O *p*-PDOS (bottom). (A Gaussian broadening of 1 eV full width at half maximum was applied to the calculated DOS. The ordinate units are arbitrary.)

NES can be anticipated for a limited number of cases. Qualitative agreement on the number of intensity maxima and their relative positions, however, as necessary for the analysis of local environments, can be expected for many systems at the advantage of low computational effort, even for complex defect systems with large supercells, whose atomic structures can be determined very accurately by pseudopotential BS methods.

C. Comparison of calculated and experimental results

A direct comparison between calculated and measured spectra is complicated by deviations from ideal cases in both theory and experiment. Therefore, some conventions are briefly introduced.

The DOS were obtained by summing over energy eigenvalues $E_{n\mathbf{k}}$ on discrete meshes of $\mathbf{k}$ points in the first Brillouin zone. For comparison with the experimental spectra the energy eigenvalues were artificially broadened with Gaussian functions of 1 eV full width at half maximum. This mimics roughly damping effects within the typical energy resolution of about 0.7 to 0.8 eV attainable at the VG HB501 UX STEM.[42] The intensities in both the experimental and the calculated spectra are normalized to the highest peak at the edge onset and are given in arbitrary units.

From the theoretical side, absolute energies of the edge onsets cannot be determined due to the use of pseudopotentials. The required core levels are incorporated in the pseudopotential and are not calculated explicitly. Additionally, band gaps of insulators are systematically underestimated in the local-density approximation. A calculation of absolute edge onset energies is therefore not feasible within the present scheme. Consequently, the interpretation of EELS edge energy shifts (as described in Ref. 1, pp. 225–227) cannot be carried out in strict analogy to molecular core level spectroscopy, and a closer analysis of the recorded ELNES patterns is required. As an alternative solution, the inflection point at the edge onset[42] is arbitrarily defined as the zero point of the energy scale.

The radii of the projection spheres in the calculation of the PDOS are chosen to give the same ratios as standard ionic radii for Mg^{2+}, Al^{3+}, and O^{2-},[50,51] and they were scaled to the smallest interatomic distance to yield touching spheres. This procedure was adopted since a variation of the projection radii in an interval of ± 0.2 Å around the scaled ionic radii turned out to be of marginal influence on the PDOS intensities.

III. OXYGEN K EDGES

Both ELNES and XANES measurements have been discussed as probes for the local coordination around the scattering center, e.g., in silicates,[8] various main-group and transition-metal oxides,[7,9,52] or, recently in titanates.[53,54] In principle, all edges can be used to obtain ''fingerprints'' of the local atom arrangement,[55] but the *K* edges are probably best suited, because the initial 1*s* state is not degenerate and most strongly localized at the scattering center. This has the advantages that the 1*s* state is not involved in bonding to neighboring atoms (negligible dispersion), and that it causes no further crystal-field splittings.

A. Influence of the exchange-correlation approximations

The determination of the appropriate treatment of atom cores by ionic pseudopotentials may be crucial for the approximation of an instantaneous transition and all approaches to get beyond it. In order to assess the reliability of the effective one-electron potentials entering the scheme, for the test case of MgO four different XC functionals were employed both in the pseudopotential generation and in the self-consistent screening of the ionic pseudopotential for the DOS calculation: Slater's X_α approximation with $\alpha=1$ (hf, local Hartree-Fock approximation[32]) and $\alpha=2/3$ (xa),[32,27,56] the local-density functional (ca),[33,34] and the gradient-corrected functional (pw).[35–37]

Figure 1 displays a comparison of the oxygen *p*-PDOS obtained from self-consistent one-electron potentials with the four different XC approximations and the experimental spectrum of the O *K* edge of MgO. At first glance no differences between the calculated curves are obvious: the second, fourth, and fifth peaks of the calculated PDOS agree very well also with the respective experimental ELNES signals. Only with the hf functional the overall energy differences between the signals are slightly larger than with all other methods. The splitting between the second and the third peak is underestimated by all four XC approximations, and a shoulder is obtained instead of a distinct peak at the edge onset in the experimental spectrum. This prominent feature can be tentatively interpreted as due to a core-hole effect which can manifest as an additional excitonic peak superposed to the first structure of the ELNES. Some minor numerical differences are detectable between the results of the four XC functionals. Quantitatively, the best match for the edge onset was obtained with the xa functional. Hence, and because of its conceptual advantage for a simple justification of single-electron spectra (approximate validity of Koopman's theorem in local Hartree-Fock theory, see, e.g., Ref. 57) the xa functional was mostly used throughout the subsequent study. All results and conclusions, however, remain the same for the more sophisticated ca and pw functionals.

B. ''Fingerprinting''

A comparison of the O *K* ELNES measured for the two cubic oxides MgO and $MgAl_2O_4$ (Fig. 2, upper parts of left and middle panels) displays a rather similar four-peak pattern, whereas the spectrum for the rhombohedral crystal α-Al_2O_3 (Fig. 2, upper part of right panel) exhibits only three prominent features within the same energy range of about 30 eV above the edge onset. The amount of splitting, however, as well as the shape at the edge onset differs for MgO and spinel, because O is coordinated octahedrally in MgO, but only by a distorted tetrahedron of one Mg ion and three Al ions in spinel. This is in accordance with previous findings, attributing a noticeable shoulder A' at the very edge onset to O in (near-) tetrahedral coordination.[4,8] The relative splittings of the other three signals *A* to *C* are of comparable magnitude in the cubic oxides, displaying again the close structural relationship in the close-packed anion arrangement and confirming it to be the dominating effect on the basic ELNES features.

In the rhombohedral α-Al_2O_3 the oxygen sites are coordinated by distorted Al^{3+} octahedra[41] and the spectrum re-

TABLE I. O *K* edges for MgO, $MgAl_2O_4$, and α-Al_2O_3. A comparison of the positions of the energy-loss peaks in the experimental spectra and the maxima of the calculated *p*-PDOS at the O center is listed along with the root mean square deviations between the measured and the calculated peak positions. All energies are given with respect to the edge onset and in eV.

	MgO		$MgAl_2O_4$		Al_2O_3	
	Expt.	Calc.	Expt.	Calc.	Expt.	Calc.
A'	−2.6	−2.6	−3.4	−3.4	−1.9	−2.9
A	0.0	0.0	0.0	0.0	0.0	0.0
B	6.5	5.5	6.8	6.4	–	–
C	17.1	17.3	18.7	18.9	17.0	17.0
rms		0.3		0.1		0.3

sembles more the one of MgO with the prominent first signal being A'. The splittings between A', A, and C are comparable to the ones determined experimentally for MgO. The major difference between the hexagonal close-packed oxygen sublattice of α-Al_2O_3 and the face-centered-cubic oxygen sublattices of MgO and $MgAl_2O_4$ is the very low intensity of signal B in the case α-Al_2O_3.

Given in the lower part of Fig. 2 are the calculated unoccupied *p* PDOS at the oxygen site. For all three cases the agreement between the calculated and the measured data is remarkably good. Not only are the rough peak patterns reproduced, but even the peak splittings and the intensity ratios of the features within the spectra are in rather close accordance with the measured data. A direct comparison of the peak positions along with the root mean square deviations (rms) between calculated and measured maxima is given in Table I. Especially the rms values for the cubic oxides are extraordinarily small with 0.1 eV and 0.2 eV, respectively, i.e., 1.0% and 0.5% of the total energy range analyzed. For the case of α-Al_2O_3 the deviation amounts still to only about 1.5% of the whole ELNES region under investigation.

From these results we conclude that the main features in the ELNES of a strongly scattering anionic center are dominated by the spatial arrangement of the surrounding strongly scattering anionic centers. Even the basic peak splitting is of comparable magnitude for all three oxides. The tiny details, on the other hand, such as intensity ratios and smaller splittings at a sub-eV to few-eV scale are determined mainly by the cation arrangement within the crystal.

IV. CATION *K* AND $L_{2,3}$ EDGES

The same treatments as described for O *K* edges in the preceding section were carried out for the metal edges, as well. As for the O *K* edge, differences between the cation PDOS obtained with the four XC approximations could hardly be determined by visual inspection. (Therefore they are not displayed here.)

A. Consideration of core-hole effects

The cation *K* edges occur at electron-energy losses above 1000 eV (Mg, 1305 eV, Al 1560 eV) (see, e.g., Refs.17 and 20), i.e., at rather high energies compared to the O *K* edges, which are recorded around 530 eV in the oxides of the present study. Thus, changes in the electronic structure at the metal centers are more pronounced than the ones at O centers, and may no longer be neglected as in the BS calculation for the electronic ground state of the solid. Differences between calculated and measured data occur especially in the energy region around the edge onset, where the measured Mg *K*-edge spectrum of MgO displays a prominent, spiky feature, and also the Al *K* edge of α-Al_2O_3 starts off with a distinct steep peak (see the experimental spectra displayed in Figs. 3 and 5 for Mg and Al *K* edges, respectively).

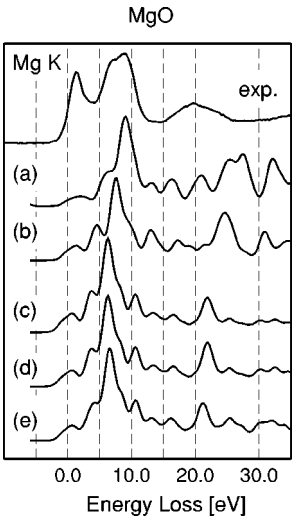

FIG. 3. Core-hole effect on the Mg *K* edge in MgO. The experiment and the unoccupied Mg *p*-PDOS for the following potentials at the Mg center are compared: (a) V(Mg), (b) V_1, (c) V_2, (d) V_3, and (e) V(Al). For details on the potential generation, see Sec. IV A.

In the literature this first peak has been ascribed to the formation of excitonic states at the scattering center as a local reaction of the electron system on the excitation of a core electron.[9,17,20,55,58] The reduced screening of the nuclear potential causes a shift of the conduction-band states to lower energies, which then split from the band manifold as localized states with negligible dispersion.[59,60] This effect becomes most prominent in *K* edges because the excitation of a 1s electron affects the screening of the nuclear potential most strongly. In an extreme picture the valence electrons feel a potential of the nucleus like that of an atom of the next element in the Periodic Table with one additional proton.[58]

In MS calculations this picture has been adopted by substituting the atom at the scattering center with the next higher element. This so-called $Z+1$ approximation (Z is the nuclear charge) has been successfully employed in the calculation of numerous *K* edges leading to a better reproduction of the very sharp feature at the edge onset in many cases, provided the cluster size was sufficiently large.[53,58,61]

In a recent BS investigation (using a linear muffin-tin orbital method) core-hole effects were included by exciting one core electron to previously unoccupied states and keeping the occupancy of the core level fixed during the self-consistent field calculations.[18] This procedure, however, did not lead to the reproduction of the spike at the edge onset, but only to a decrease of the band gap and a diminishing of the conduction-band width.

Both approaches were applied to MgO as a test case. In addition to the substitution of Mg by Al in the $Z+1$ approximation, norm-conserving ionic pseudopotentials were generated for the following core-hole excitations of the Mg atom:

$$V_1: \mathrm{Mg}(1s^2 2s^2 2p^6 3s^2) \rightarrow \mathrm{Mg}^*(1s^{1.5} 2s^2 2p^6 3s^2 3p^{0.5}),$$

$$V_2: \mathrm{Mg}(1s^2 2s^2 2p^6 3s^2) \rightarrow \mathrm{Mg}^*(1s^1 2s^2 2p^6 3s^2 3p^1),$$

$$V_3: \mathrm{Mg}(1s^2 2s^2 2p^6 3s^2) \rightarrow \mathrm{Mg}^+(1s^1 2s^2 2p^6 3s^2) + 1e^-.$$

The generation of pseudopotential V_1 is motivated by Slater's transition-state concept for the treatment of low-energy excitations within the ground-state density-functional theory.[62,63] This procedure is necessary, because density-functional theory, given by the two theorems of Hohenberg and Kohn, strictly applies only to the ground state of an electron system in a given external potential, e.g., by the nuclei.[26] Therefore, in principle excitation energies cannot be calculated in analogy to Hartree-Fock theory as the difference between the total energies of electronic ground and excited states or equally from the one-electron orbital energies via Koopmans' theorem.[57] Slater demonstrated, however, that the excitation of only half of an electron can still be performed within the limitations of a ground-state theory. The resulting electron density and potential V_1 incorporate already some final state effects of the excitation, although to a lower degree than the full $1s \rightarrow 3p$ process would do.

The construction of the second and the third pseudopotentials V_2 and V_3 strictly violates the basic principles of density-functional theory. For V_2 a whole $1s$ electron is excited to the previously empty atomic $3p$ states, leaving a complete hole in the $1s$ core shell. In V_3 the removal of the core electron by cation formation deviates even more from the ground state. With the help of V_3 an upper bound for the effects of a full $1s$ core ionization at the Mg center is estimated. By additional comparison to calculations on ground-state MgO with the pseudopotential $V(\mathrm{Mg})$ and the hypothetical isostructural compound AlO [with $V(\mathrm{Al})$] the amount of unscreening of the nucleus can be studied stepwise in increasing order $V(\mathrm{Mg}) < V_1 < V_2 < V_3 \approx V(\mathrm{Al})$. ($<$ and $\approx$ symbolize the strength ratios of the core-hole excitations.)

Figure 3 shows a compilation of the experimental Mg K edge in MgO and the calculated p-projected densities of states (p-PDOS) on Mg, employing the pseudopotentials for the five reference atoms in the following order: for the ground-state Mg atom (a), for the three excited Mg atoms with V_1 (b), V_2 (c), and V_3 (d), and for the ground-state Al atom (e).

As stated previously, the peak positions of the experimental spectrum (uppermost curve) and the ground-state MgO p-PDOS (a) are in quite good agreement, but the peak shapes and intensities differ especially at the edge onset. With the pseudopotential V_1 only minor changes occur: The second prominent feature in the spectrum (b) gains more intensity compared to the pure $V(\mathrm{Mg})$ case (a) and the features at higher energy loss match better. The sharp peak at the edge onset, however, is not reproduced. Upon further exciting the full electron from $1s$ to $3p$ with V_2 the observed changes become more pronounced (c), but, as noted previously for transition-metal silicides,[18] the only consequences are a further narrowing of the conduction-band width and a slight diminishing of the band gap. With the ion pseudopotential V_3 the same result is obtained (d).

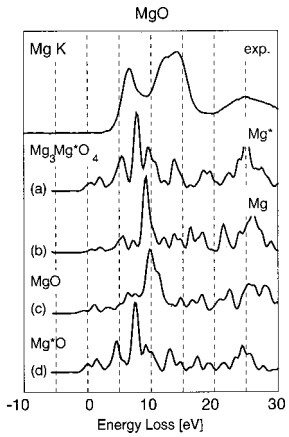

FIG. 4. Core-hole effect on the Mg K edge in MgO studied with a $Mg_3Mg^*O_4$ supercell, compared to MgO and Mg^*O unit cells. (A Gaussian broadening of 0.25 eV was employed.)

It is worth noting that the PDOS (e) calculated with the $Z+1$ approximation exhibits the same peak positions and intensities as the PDOS obtained with the potentials V_2 and V_3, for which one electron is missing in the $1s$ shell. On the one hand this result confirms that the $Z+1$ approximation is a good qualitative description of the core-hole effect in K edges, justifying its use in MS calculations (see, e.g., Ref. 17). On the other hand it means that the introduction of the core hole in the band-structure calculation, at least for small unit cells like $(\mathrm{MgO})_1$, is not sufficient to reproduce the first sharp feature at the edge onset. Comparing the Mg p-PDOS to the Mg L_1 edge in MgO (see also Ref. 17) the agreement in intensities is significantly improved. The L_1 edge displays only a small peak at the edge onset, but the number and energy spacings of the peaks are identical to the K edge and in good agreement with the band-structure data.

In MS calculations the intensity differences between K and L_1 emerged only with increasing cluster size, when both the excited Mg atom in the cluster center and the nonexcited Mg atoms in the surrounding shells were present.[17] Analogous to this investigation, a small simple-cubic supercell of the size $(\mathrm{MgO})_4$ was calculated with the mixed-basis method, using three times $V(\mathrm{Mg})$ and once V_1 for the cations ($Mg_3Mg^*O_4$). To allow a more detailed analysis, a smaller Gaussian broadening of 0.25 eV was used here. The corresponding Mg p-PDOS data are shown in Fig. 4, where Mg denotes the PDOS of the ground-state Mg center and Mg* the PDOS of the excited Mg center. For the Mg* centers the difference between the small cell (d) and the supercell (a) are not pronounced. The major improvement appears for the second group of peaks at a 7–10 eV energy loss, whereas the edge onset is virtually unchanged. The p-PDOS of the ground-state Mg center in $Mg_3Mg^*O_4$ changes slightly compared to the p-PDOS of pure MgO [cf. Fig. 4, curves (b) and (c)]. This finding indicates that the influence of the centers with the modified core-hole potential V_1 is not yet sufficiently screened at the nearest-neighboring ground-state Mg site. Visible by the small differences between curves (a) and (d) there is some artificial superlattice inter-

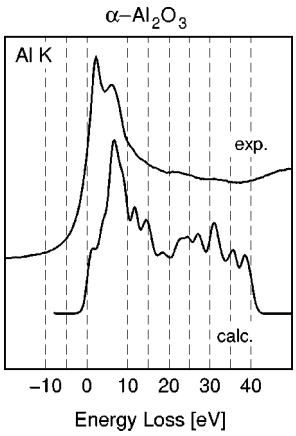

FIG. 5. Experimental *K* edge and calculated *p*-PDOS of Al in α-Al_2O_3.

action between two excited next-nearest-neighbor Mg sites in the $Mg_3Mg^*O_4$ model. As the experimental recording conditions ensure that two excitation processes are independent from each other, a thorough treatment of the core-hole effect requires the use of large and computationally intensive supercells. This, however, is beyond the scope of the present investigation on the abilities and limitations of a simple and quick scheme for the interpretation of EELS.

The analysis of the Al *K* edge in α-Al_2O_3 yields a similar picture. As displayed in Fig. 5, the corresponding measured spectrum reveals only a few distinct features. The splitting of the first peak is found already in the ground-state calculation with reasonable accuracy.

B. Account for crystal-field symmetry

For the L_2 and L_3 edges of the third-row metals Mg and Al the core relaxation effects are of less importance, because the corresponding excitation processes for the $2p \rightarrow 3s;\ 3d$ transitions are low in energy [Mg: 51 eV, Al: 78 eV (Refs. 17 and 20)]. In this case the major complication with respect to the calculation is the large number of 18 different possible one-electron excitations from the three *p* states into the six *s* and *d* states at the scattering center. For a nonrelativistic free atom all initial and all final states, respectively, would be degenerate with respect to the magnetic quantum number *m* for a given value of the angular-momentum quantum number *l*. Two types of interactions lift these degeneracies for a relativistic atom in a crystal. The initial $2p$ core states are split by the spin-orbit interaction which gives rise to the energy difference between the L_3 and the L_2 edge. In free Mg or Al atoms this splitting was determined as only 0.4 eV from a self-consistent Dirac-Fock-Slater calculation employing the same XC functional as used in the BS calculations for the oxide crystals. Optical measurements on α-Al_2O_3 with a synchrotron light source yielded the same splitting of the first peak in the Al $L_{2,3}$ edge by 0.4 eV, which was attributed to the spin-orbit splitting of the $2p$ states.[64] However, this amount is below the experimental energy resolution of an EELS experiment and is presently neglected. The calculated edges will therefore be denoted as ''$L_{2,3}$'' in the following, although they are not corrected for the $2p_{3/2}$-$2p_{1/2}$ splitting and strictly correspond only to a L_3 or a L_2 edge.

Both the core and the conduction-band states can be split additionally into subsets of different symmetries due to the influence of the crystal environment, which lifts the degeneracy with respect to the magnetic quantum number *m*. In analogy to optical spectroscopy, not all possible transitions between these subsets contribute to the ELNES. Some of the subsets cannot interact with one another for symmetry reasons, thus the corresponding transition-matrix elements vanish. As pointed out in Ref. 23, however, the sum over projections onto partial waves for the momenta $l=0$ and $l=2$ is a reasonable approach in the case of main-group metals, since both the $3d$ and the $4s$ states are diffuse (no white lines) and have comparable overlap with the $2p$ core state. The *l* dependence of the transition matrix element may therefore be neglected.

The influence of the crystal field can be accounted for as follows. Both the initial- and the final-state levels are split into manifolds belonging to one of the irreducible representations of the local point-symmetry group at the scattering center. The determination of the correct point group may be complicated by the fact that the *z* axis is already fixed by the direction of the incident electron beam. If this *z* axis and the principal rotation axis of the local point group do not coincide, this leads to a symmetry reduction which must be accounted for. From the orthogonality theorem for the combination of representations it follows that electronic transitions between two states have a nonvanishing contribution only if the integrand of the transition matrix element belongs to the totally symmetric representation of the point group (for a detailed description see, e.g., Ref. 65, pp. 20–25 and 80–82). Otherwise, positive and negative contributions in the integration cancel due to symmetry reasons. Instead of calculating the full matrix element it is sufficient to form a reducible representation from the irreducible representations of the initial state, the dipole operator, and the final state, which can be decomposed into irreducible representations. If the totally symmetric representation contributes, the corresponding excitation is allowed by symmetry, and the matrix element is arbitrarily chosen as 1. All other matrix elements are set to zero.

In the following the local coordinate system is chosen with the *z* axis parallel to the direction of the incident electron beam. From the nominally $3\times5=15$ transition processes from *p* to *d* states, only nine can be achieved, obeying the selection rule $\Delta m=0,\pm1$. The allowed transitions are schematically given in Fig. 6(a) where a horizontal arrow depicts an excitation to the $m=0$ component, and the arrows pointing up and down are symbols for excitations to the $m=\pm1$ components, respectively. Thus for the $L_{2,3}$ edges the projections to spherical harmonics Y_{2m} should be added up including to corresponding weights, i.e., the ratio Y_{2-2}: Y_{2-1}: Y_{20}: Y_{21}: Y_{22} should be 1:2:3:2:1. Note, however, that all $p \rightarrow s$ transitions are allowed.

In another step, the interaction with the incident electron beam is reconsidered. The dipole selection rule was derived under the assumption that the scattering angle is small, and ideally the spectrum is recorded under parallel scattering conditions. In this limit only the *z* component of the dipole operator contributes, whereas the *x* and *y* components can be neglected as they are perpendicular to the electron beam. This situation may be compared to the use of longitudinally

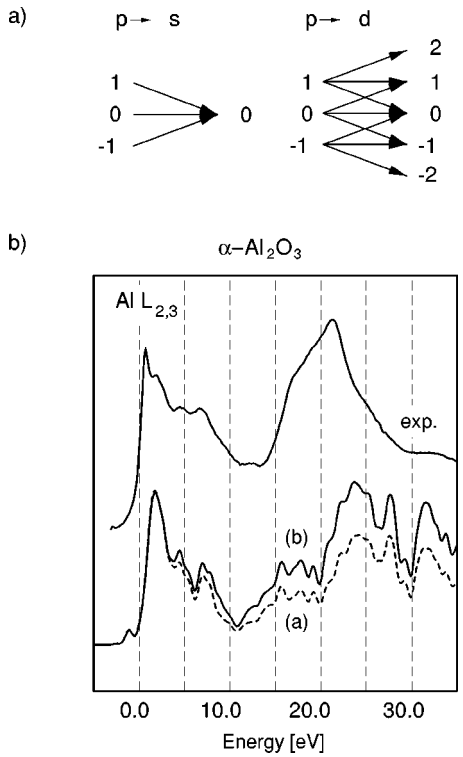

FIG. 6. (a) Schematic diagram of all symmetry-allowed $p \rightarrow s$ and $p \rightarrow d$ transitions contributing to the Al $L_{2,3}$ edge. (b) Al $L_{2,3}$ edge in α-Al_2O_3. The experimental ELNES is compared to the simple sum of unoccupied Al *s* and *d* PDOS (a). The result of the weighting procedure explained in Sec. IV B is given by curve (*b*). (A Gaussian broadening of 0.25 eV was employed in the calculation.)

polarized light in optical spectroscopy. Evidence for intensity changes with the polarization direction is given by synchrotron-light spectra recorded by Tomiki *et al.*[64] for the highly anisotropic material α-Al_2O_3. Therefore, the Al $L_{2,3}$ edge in α-Al_2O_3 was chosen for such a further investigation.

Figure 6(b) displays the experimental Al $L_{2,3}$ edge, the equally weighted sum of the Al *s*- and *d*-PDOS [dashed line (a)] and a sum weighted by the matrix elements according to the irreducible representations in parallel scattering conditions, as described above [solid line (b)]. Concerning the number and positions of the peaks, already the equally weighted sum and the experimental spectrum agree very well, especially in the first ten eV from the edge onset, where the PDOS is dominated by the *s* contribution. The agreement is still quite good also in the higher-energy part of the spectrum up to the L_1-edge onset, where the *d* contribution prevails. Major discrepancies occur around 20 eV energy loss, where one huge, featureless peak is observed in the experiment, whereas the calculation shows more structure and lower intensity. The peak position cannot be changed by the weighting procedure outlined above, but only the intensity ratios of already existing features. For the Al $L_{2,3}$ edge, however, it leads to a noticeable improvement, when only the transitions allowed within C_{3v} symmetry around the Al center are taken into account [see Fig. 6(b)].

V. SUMMARY

A theoretical scheme based on Fermi's golden rule was presented for the calculation and analysis of near-edge structures in electron-energy-loss spectra by means of site- and angular-momentum-projected densities of states obtained from crystal-electron band structures. The band structures were calculated *ab initio*, based on density-functional theory, employing a mixed basis of plane waves and local orbitals to represent the valence electron wave functions, and norm-conserving *ab initio* pseudopotentials for the core-valence interaction. Both the efficiency and the limitations of this approach were discussed in detail.

The application of this scheme to the main-group-metal oxides MgO, α-Al_2O_3, and $MgAl_2O_4$ supports the concept of fingerprinting with the O *K* edge. Very good agreement between calculated and measured data is obtained with respect to the following criteria: Number of maxima or shoulders, positions and intensity ratios of the peaks. The spatial arrangement of the strongly scattering anions determines the basic ELNES features such as the number and the positions of the peaks. The additional fine structure superimposed on the prominent peaks as well as the intensity ratios, on the other hand, are caused by the symmetry of the cation sublattice and the related crystal-field effects.

An analysis of the cation ELNES in MgO and α-Al_2O_3 by a straightforward comparison with the corresponding local site- and angular-momentum projections of densities of unoccupied states yielded less satisfactory results. The discrepancies were attributed to the effect of core-hole relaxation in the case of the *K* edges and to the influence of the crystal field on the more complicated excitation processes involved in the $L_{2,3}$ edges.

To check relaxation effects caused by the core hole, the Mg *K* edge of MgO was recalculated with a series of pseudopotentials, which were generated for different atomic reference configurations of Mg. The conduction band became contracted and the band gap slightly diminished. The experimentally observed sharp peak at the edge onset, however, was not yet reproduced. The use of a small supercell did not improve the result significantly. It merely indicated a considerable screening range of the excited core. It is concluded that the shape of energetically high *K* edge onsets is not easily obtained on the basis of the effective one-electron approach used here, unless larger supercells are employed.

The matrix-element contribution for cation $L_{2,3}$ edges was reexamined, since many different excitation processes from the $2p$ to the $(3d+3s/4s)$ states may contribute to the intensity of these edges. Some of the transitions are forbidden due to local-symmetry constraints imposed by the selection rule $\Delta m = 0, \pm 1$, and the condition of near-parallel scattering. The matrix elements for all remaining allowed transitions were chosen as equal. The Al $L_{2,3}$ edge of α-Al_2O_3 was investigated as a test case because of the larger anisotropy of this material compared to the cubic MgO, and the corresponding low local symmetry. Already an equally weighted sum of the *s*-PDOS and the *d*-PDOS agreed rather nicely with the measured data. If the corrections for the proper weighting factors of the DOS projections were included into the calculated spectrum, an additional improvement of the intensity ratios in the Al $L_{2,3}$ edge was achieved.

Elaborations of the methodology and its application to ELNES and the local bonding at interfaces in ceramics are in progress. One principal goal of the present study was to make the methodology as simple as possible both conceptually, e.g., by using X_α together with more sophisticated XC approximations, and computationally, e.g., by avoiding an explicit calculation of transition matrix elements. This makes the approach immediately suitable, in connection with pseudopotential total-energy and force calculations for large-supercell systems, as a quick *a posteriori* analysis tool for local electronic structure and bonding.

ACKNOWLEDGMENTS

The present work was supported by the Volkswagen Stiftung, Germany, through Project No. VW I/70502. For providing the displayed experimental spectra the authors thank H. Müllejans (O *K* and cation-$L_{2,3}$ edges) and G. Duscher (cation-*K* edges). They appreciate many valuable discussions on EELS experiments, calculations, and interpretations with H. Müllejans, G. Duscher, M. Gülgün, W. Y. Ching, T. Ochs, and A. Levay.

[1] R.F. Egerton, *Electron Energy-Loss Spectroscopy in the Electron Microscope* (Plenum Press, New York, 1996).
[2] F. Hofer, P. Warbichler, and W. Grogger, Ultramicroscopy **59**, 31 (1995).
[3] G. Duscher, N.D. Browning, and S.J. Pennycook, Phys. Status Solidi A **166**, 327 (1998).
[4] J. Bruley, M.-W. Tseng, and D.B. Williams, Microsc. Microanal. Microstruct. **6**, 1 (1995).
[5] C. Scheu *et al.*, Microsc. Microanal. Microstruct. **6**, 19 (1995).
[6] Y. Ikuhara, Y. Sugawara, I. Tanaka, and P. Pirouz, Interface Sci. **5**, 5 (1997).
[7] S.P. Kowalczyk, F.R. McFeely, L. Ley, and V.T. Gritsna, Solid State Commun. **23**, 161 (1977).
[8] J. Tafto and J. Zhu, Ultramicroscopy **9**, 349 (1982).
[9] C. Colliex, T. Manoubi, M. Gasgnier, and L.M. Brown, Scanning Electron. Microsc. **II**, 489 (1985).
[10] M. Inokuti, Rev. Mod. Phys. **43**, 297 (1971).
[11] X. Weng, P. Rez, and O.F. Sankey, Phys. Rev. B **40**, 5694 (1989).
[12] G.A. Sawatzky, Microsc. Microanal. Microstruct. **2**, 153 (1991).
[13] J. Fink, in *Unoccupied Electronic States: Fundamentals for XANES, EELS, IPS, and BIS*, edited by J. C. Fuggle and J. E. Inglesfield (Springer-Verlag, Berlin, 1992), Vol. 69, Chap. 7.
[14] P.J. Durham, J.B. Pendry, and C.H. Hodges, Comput. Phys. Commun. **25**, 193 (1982).
[15] D.D. Vvedensky, D.K. Saldin, and J.B. Pendry, Comput. Phys. Commun. **40**, 421 (1986).
[16] C.R. Natoli, M. Benfatto, and S. Doniach, Phys. Rev. A **34**, 4682 (1986).
[17] T. Lindner, H. Sauer, W. Engel, and K. Kambe, Phys. Rev. B **33**, 22 (1986).
[18] P. Lerch *et al.*, Phys. Rev. B **45**, 11 481 (1992).
[19] P.E. Batson, Phys. Rev. B **47**, 6898 (1993).
[20] R.H. French, D.J. Jones, and S. Loughin, J. Am. Ceram. Soc. **77**, 412 (1994).
[21] I. Tanaka and H. Adachi, J. Phys. D **29**, 1725 (1996).
[22] P. Rez, J.M. MacLaren, and D.K. Saldin, Phys. Rev. B **57**, 2621 (1998).
[23] D.A. Muller, D.J. Singh, and J. Silcox, Phys. Rev. B **57**, 8181 (1998).
[24] J. Kübler and V. Eyert, in *Electronic Structure Calculations*, edited by K.H.J. Buschner (Verlag Chemie, Weinheim, 1992), p. 1.
[25] W.E. Pickett, Comput. Phys. Rep. **9**, 115 (1989).
[26] P. Hohenberg and W. Kohn, Phys. Rev. **136**, B864 (1964).
[27] W. Kohn and L.J. Sham, Phys. Rev. **140**, A1133 (1965).
[28] S.G. Louie, K.M. Ho, and M.L. Cohen, Phys. Rev. B **19**, 1774 (1979).
[29] C.L. Fu and K.M. Ho, Phys. Rev. B **28**, 5480 (1983).
[30] C. Elsässer *et al.*, J. Phys.: Condens. Matter **2**, 4371 (1990).
[31] B. Meyer, C. Elsässer, and M. Fähnle, FORTRAN90 Program for Mixed-Basis Pseudopotential Calculations for Crystals, Max-Planck-Institut für Metallforschung, Stuttgart (unpublished).
[32] J.C. Slater, Phys. Rev. **81**, 385 (1951).
[33] J.P. Perdew and A. Zunger, Phys. Rev. B **23**, 5048 (1981).
[34] D.M. Ceperley and B.J. Alder, Phys. Rev. Lett. **45**, 566 (1980).
[35] J.P. Perdew, Phys. Rev. B **33**, 8822 (1986).
[36] J.P. Perdew, Phys. Rev. B **34**, 7406 (1986).
[37] J.P. Perdew and Y. Wang, Phys. Rev. B **33**, 8800 (1986).
[38] D. Vanderbilt, Phys. Rev. B **32**, 8412 (1985).
[39] R. W. G. Wyckoff, *Crystal Structure* (Interscience Publishers, New York, 1965), Vol. 1.
[40] N.G. Zorina and S.S. Kvitka, Kristallografiya **13**, 703 (1968).
[41] W.E. Lee and K.P.D. Lagerlöf, J. Electron Microsc. Tech. **2**, 247 (1985).
[42] H. Müllejans and J. Bruley, Ultramicroscopy **53**, 351 (1994).
[43] L. Hedin, Phys. Rev. **139**, A796 (1965).
[44] M.S. Hybertsen and S.G. Louie, Phys. Rev. Lett. **55**, 1418 (1985).
[45] M.S. Hybertsen and S.G. Louie, Comments Condens. Matter Phys. **13**, 223 (1987).
[46] P. Fulde, *Electron Correlations in Molecules and Solids* (Springer, Berlin 1993), Ch. 9.
[47] B. Kralik, E.K. Chang, and S.G. Louie, Phys. Rev. B **57**, 7027 (1998).
[48] B. Meyer, K. Hummler, C. Elsässer, and M. Fähnle, J. Phys.: Condens. Matter **7**, 9201 (1995).
[49] C.J. Pickard, Ph.D. thesis, University of Cambridge, 1997.
[50] A. Bondi, J. Phys. Chem. **68**, 441 (1964).
[51] R.D. Shannon, Acta Crystallogr., Sect. A: Cryst. Phys., Diffr. Theor. Gen. Crystallogr. **32**, 751 (1976).
[52] R.D. Leapman, L.A. Grunes, and P.L. Fejes, Phys. Rev. B **26**, 614 (1982).
[53] F. Farges, G.E. Brown, and J.J. Rehr, Phys. Rev. B **56**, 1809 (1997).
[54] Z.Y. Wu, G. Ouvrard, P. Gressier, and C.R. Natoli, Phys. Rev. B **55**, 10 382 (1997).
[55] R. Brydson, H. Sauer, W. Engel, and E. Zeitler, Microsc. Microanal. Microstruct. **2**, 159 (1991).
[56] K. Schwarz, Phys. Rev. B **5**, 2466 (1972).
[57] A. Szabo and N.S. Ostlund, *Modern Quantum Chemistry, Introduction to Advanced Electronic Structure Theory* (McGraw-Hill, New York, 1989).

[58] H.P. Hjalmarson, H. Büttner, and J.D. Dow, Phys. Rev. B **24**, 6010 (1980).
[59] R.S. Knox, Solid State Phys. **5**, 1 (1963).
[60] M. Ueta *et al.*, in *Excitonic Processes in Solids*, edited by M. Cardona, P. Fulde, K. von Klitzing, and H. J. Kneisser (Springer, New York, 1986).
[61] R. Brydson, H. Sauer, W. Engel, and F. Hofer, J. Phys.: Condens. Matter **4**, 3429 (1992).
[62] J.C. Slater, Adv. Quantum Chem. **6**, 1 (1972).
[63] R.G. Parr and W. Yang, *Density-Functional Theory of Atoms and Molecules* (Oxford University Press, New York, 1989).
[64] T. Tomiki *et al.*, J. Phys. Soc. Jpn. **62**, 1372 (1993).
[65] M. Tinkham, *Group Theory and Quantum Mechanics* (McGraw-Hill, New York, 1965).